Earth and Planetary Science Letters 288 (2009) 126–131

Contents lists available at ScienceDirect

Earth and Planetary Science Letters

journal homepage: www.elsevier.com/locate/epsl

# Geodetic exploration of the elastic properties across and within the northern San Andreas Fault zone

R. Jolivet [a,*,1], R. Bürgmann [b,*], N. Houlié [b,2]

[a] Laboratoire de Géologie, Ecole Normale Supérieure, CNRS UMR 8538, Paris, France
[b] Berkeley Seismological Laboratory, University of California, Berkeley, Berkeley, California, USA

ARTICLE INFO

*Article history:*
Received 23 June 2009
Received in revised form 4 September 2009
Accepted 8 September 2009
Available online 4 October 2009

Editor: Y. Ricard

*Keywords:*
San Andreas Fault
San Francisco Bay Area
GPS
interseismic
heterogeneous dislocation models

ABSTRACT

Relying on densely spaced GPS data collected between 1996 and 2007 and on InSAR data spanning the 1992–2001 time period, we explore the effects of lateral rheological heterogeneities across the San Andreas Fault near Point Reyes on the interseismic velocity field. We evaluate heterogeneous elastic dislocation models, including an asymmetric model with contrasting rigidities on either side of the San Andreas Fault and models with a narrow compliant fault zone that lead to high near-fault strain rates. We show that we cannot resolve a compliant zone from interseismic surface displacement measurements unless independent constraints on the locking depth exist. We infer an $18 \pm 1$ mm yr$^{-1}$ slip rate on the San Andreas Fault with a $10 \pm 2$ km locking depth and a 40% higher rigidity to the SW of the fault. At Bodega Bay, GPS and EDM data suggest a compliant zone on the SAF with a 50-to-60% rigidity decrease, but 25 km further south we find no evidence for a weak fault zone. This suggests substantial variability in fault zone properties along the San Andreas Fault.

Published by Elsevier B.V.

## 1. Introduction

Earthquake cycle deformation is commonly modelled assuming laterally homogeneous elastic properties in the Earth's crust. Interseismic deformation models are often based on an elastic half-space, sliced by an infinitely deep and infinitely long dislocation below seismogenic depth (Savage and Burford, 1973). First-order variations in rock elastic strength both across and within fault zones can strongly impact inferences of fault slip parameters and earthquake rupture characteristics in a homogeneous model (Ben-Zion and Huang, 2002; Le Pichon et al., 2005; Schmalzle et al., 2006; Barbot et al., 2008). Here we focus on the effects of such lateral rheological variations across and within the San Andreas Fault (SAF) zone on the interpretation of space geodetically measured surface deformation.

The Northern San Francisco Bay Area (Fig. 1) is sliced by three major right-lateral strike-slip faults, the northern SAF, the Rodgers Creek fault and the Green Valley fault. The Rodgers Creek fault represents the North Bay continuation of the Hayward fault zone and the Green Valley fault is the northern extension of the Concord fault. North of the juncture with the San Gregorio fault, geodetic and geologic data suggest a SAF slip rate of 20–25 mm yr$^{-1}$ (Lisowski et al., 1991; d'Alessio et al., 2005). At a geological time scale, the study of stream-channel deposit offsets, 45 km north of San Francisco, provides a minimum value for the late Holocene slip rate of $24 \pm 3$ mm yr$^{-1}$ (Niemi and Hall, 1992). The remainder of the 40 mm yr$^{-1}$ of Pacific plate to Sierra Nevada Great Valley microplate motion is primarily accommodated by the Rodgers Creek and the Green Valley faults. Both the Rodgers Creek fault (Funning et al., 2007) and the Green Valley fault (MacFarland et al., 2007) accommodate some of their shallow slip budget by aseismic creep.

Near Point Reyes, the SAF separates two different geologic terranes. On the east side of the fault is the Franciscan Complex, made of a mixture of Mesozoic oceanic crustal rocks and sediments, which were accreted onto the North American continent during subduction of the Farallon plate. On the west side of the SAF lies the Salinian terrane, which is composed of Cretaceous granitic and metamorphic rocks, overlain by Tertiary sedimentary rocks and Quaternary fluvial terraces.

Prescott and Yu (1986) and Lisowski et al. (1991) describe an asymmetric deformation pattern along a trilateration-measured surface velocity profile across the SAF at Point Reyes, which can be explained by higher rigidities to the SW of the fault. (Le Pichon et al., 2005), describe an asymmetric pattern further north along the SAF at Point Arena, but do not find significant asymmetry in the GPS data set of Savage et al. (2004) at Point Reyes. Chen and Freymueller (2002) rely on near-fault strain rates determined from trilateration and GPS measurements to infer a 2-km-wide, near-fault compliant zone with 50% reduced rigidity, describing this contrast as starting in Bodega Bay and increasing further south. Here we

* Corresponding authors.
*E-mail addresses:* romain.jolivet@ujf-grenoble.fr (R. Jolivet), burgmann@seismo.berkeley.edu (R. Bürgmann), earnh@leeds.ac.uk (N. Houlié).
[1] Now at Laboratoire de Geophysique Interne et Tectonophysique, Université Joseph Fourier, Grenoble, France.
[2] Now at School of Earth and Environment - Institute of Geophysics and Tectonics, University of Leeds, Leeds, UK.

0012-821X/$ – see front matter. Published by Elsevier B.V.
doi:10.1016/j.epsl.2009.09.014

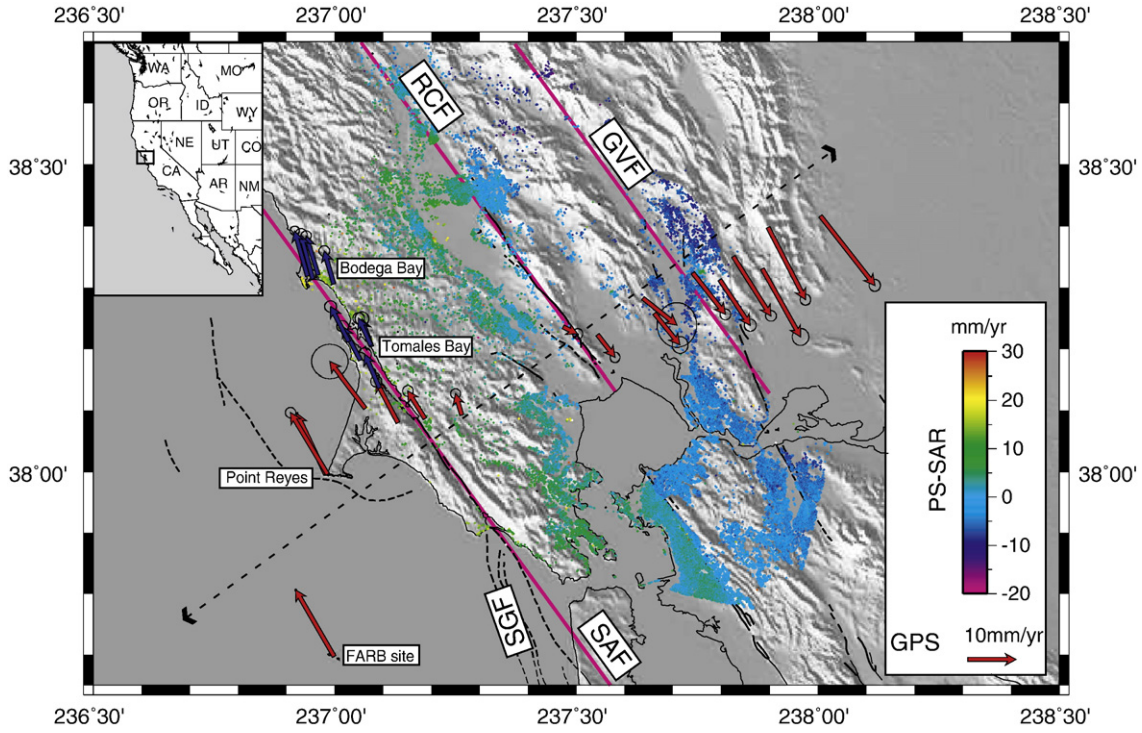


**Fig. 1.** Map and SRTM topography of the northern Bay Area, California, USA. The blue arrows are the data calculated from 1996, 2000 (Chen and Freymueller, 2002) and 2007 (this study) GPS campaign measurements. The red arrows are from the BAVU 2 compilation. The colored dots are the along SAF strike projected horizontal velocities derived from PS-InSAR data from Funning et al. (2007). The black dashed arrow spans the studied Point Reyes profile shown in Fig. 3. Mapped fault traces are shown by black lines while the three modelled faults are in purple (SAF, GVF and RCF).

use densely spaced GPS velocities, permanent scatterer InSAR data and EDM measurements across the SAF to constrain models of the interseismic elastic loading in this area and evaluate changes in elastic properties across and within the fault zone.

## 2. Semi-infinite elastic media deformation models

### 2.1. Homogeneous elastic half-space

The classic way to interpret a GPS-derived velocity profile across a strike-slip fault is to use the screw dislocation model (Chinnery, 1961; Savage and Burford, 1973):

$$V(y) = \frac{V_T}{\pi} atan(\frac{y}{D}), \tag{1}$$

where $V$ is the predicted fault-parallel velocity of a surface point at distance $y$ from the fault and $V_T$ is the fault slip rate below the locking depth $D$ and equals the far field plate velocity. This model assumes an infinite dislocation buried in a semi-infinite elastic medium. Next we consider laterally heterogeneous models that account for variations of elastic properties across and within the fault zone. We will consider here only the variations of the Young's modulus $E$, which is related to the shear modulus $G$ as $E=2G(1+\nu)$, where $\nu$ is Poisson's ratio.

### 2.2. Asymmetric elastic half-space

As the SAF separates two different geologic terranes, we first consider the model developed by (Le Pichon et al., 2005) where the fault separates two elastic blocks with different Young's moduli $E_1$ and $E_2$ and a velocity ratio, $K = \frac{V_1}{V_1 + V_2}$, where $V_1$ is the far field velocity with respect to the fault for $y<0$ and $V_2$ the far field velocity with respect to the fault for $y>0$, in the following equations:

$$\begin{aligned} y<0 \Rightarrow V(y) &= \frac{2KV_T}{\pi} atan(\frac{y}{D}) \\ y>0 \Rightarrow V(y) &= \frac{2(1-K)V_T}{\pi} atan(\frac{y}{D}), \end{aligned} \tag{2}$$

where $V(y)$ is again the velocity at a distance $y$ from the fault, $V_T = V_1 + V_2$ is the fault slip rate, and $D$ is the locking depth. The velocity ratio $K$ is equivalent to the ratio $\frac{E_2}{E_1 + E_2}$. If the creeping dislocation is shifted a few kilometers away from the rigidity discontinuity, the velocity ratio $K$ used in Eq. (2) changes while the rigidity ratio is constant (Jolivet et al., 2008). We will here consider that the deep creeping dislocation is located right under the rigidity discontinuity, which represents the fault.

### 2.3. Compliant fault zone model

We also evaluate the deep Compliant Fault Zone Model (CFZM) developed in Chen and Freymueller (2002), following Rybicki and Kasahara (1977). A low-rigidity fault zone with Young's modulus $E^*$ is introduced between two elastic blocks (Fig. 2). The interseismic velocity $V$ at a distance $y$ from the fault is

$$\begin{aligned} y<-h \Rightarrow V(y) &= \frac{2(1-\kappa)V_T}{\pi} \sum_{n=0}^{\infty} \kappa^n atan(\frac{y-2nh}{2D}) \\ -h<y<h \Rightarrow V(y) &= \frac{V_T}{\pi}\left[atan(\frac{y}{2D}) + \left[\sum_{n=0}^{\infty} \kappa^n atan(\frac{y-2nh}{2D}) + \kappa^n atan(\frac{y+2nh}{2D})\right]\right] \\ y\ h \Rightarrow V(y) &= \frac{2(1-\kappa)V_T}{\pi} \sum_{n=0}^{\infty} \kappa^n atan(\frac{y+2nh}{2D}), \end{aligned} \tag{3}$$

where $\kappa = \frac{E-E^*}{E+E^*}$, $V_T$ the far field displacement, $D$ the locking depth and $2h$ the width of the compliant zone centered above the

dislocation. As shown in Fig. 2, this model tends to localize the deformation in the compliant zone. If fault zones have greatly reduced elastic strength, a high deformation gradient in the fault zone should be detected with geodetic data.

This model (A in Fig. 2) is based on an infinitely deep weak fault zone. If we consider that the fault zone is weaker than the surrounding medium because of damage caused by repeated earthquakes (Peng and Ben Zion, 2006), this zone should not extend deeper than the locking depth. Therefore, we developed a shallow CFZM whose geometry is illustrated in Fig. 2 B. Fialko et al. (2002) developed a similar shallow CFZM for the coseismic deformation case where localized deformation across two faults was induced by the 1999 Hector Mine earthquake. We consider an elastic half-space with a tabular weak zone centered on the locked fault between the surface and the locking depth. We perform the simulations using the three-dimensional finite element code ADELI (Chéry et al., 2001). We consider an elastic plate (500 km long, 400 km wide, 300 km deep) loaded with gravitational body forces and supported at its base by hydrostatic pressure. The size of the elements varies from 0.1 km close to the fault to 25 km. This plate is sliced in two parts by two juxtaposed planes where we impose a velocity condition (slip) below the locking depth. Between the surface and the locking depth these planes are coupled. We vary the ratio of the Young's moduli $\frac{E^*}{E}$ between the grey-shaded zone and the surrounding medium (B. in Fig. 2) between 0.1 and 1.

The results of the computations are presented in Fig. 2 C. for $\frac{E^*}{E} = 0.2$. The shallow CFZM tends to localize the deformation closer to the fault than the infinite CFZM. However, the difference between a shallow CFZM and a deep CFZM never exceeds 5% of the far field velocity. If we consider a mean slip rate of 20 mm$yr^{-1}$ on the SAF, the difference between a shallow CFZM and a deep CFZM will never exceed 1 mm$yr^{-1}$ which is less than the uncertainties in the GPS and SAR data. Thus, we only use the deep CFZM model in our analysis of the North Bay deformation data.

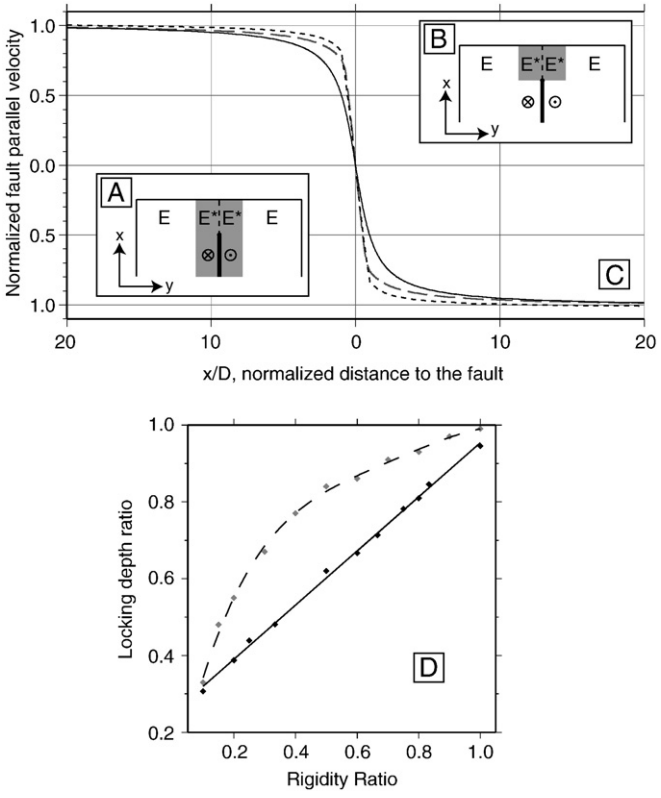


**Fig. 2.** Model geometry of A. deep and B. shallow CFZM. The shaded area is the weak fault zone. C. Comparison between a 10 km locking depth classic screw dislocation model (continuous line), a 10 km locking depth Deep CFZM (long-dashed grey line) and a 10 km locking depth Shallow CZFM (dashed black line) with rigidity in the 2-km-wide fault zone being reduced by 80%. D. Locking depth determined by fitting velocity profiles (400 km long with a point spacing of 0.5 km) calculated with the CFZMs with the half-space Eq. (1). The locking depth ratio is the ratio between the homogeneous model fitted locking depth and the computed CFZM locking depth. The grey dots are the best-fit locking depth for the deep CFZM and the dashed line is the corresponding polynomial fit. The black dots are the fitted locking depth for the shallow CFZM and the continuous line is the corresponding linear fit.

We tried to fit the computed velocity profiles obtained with both CFZMs with the classic half-space dislocation model, to evaluate the trade-off between the rigidity ratio and the obtained best-fit locking depth in a homogeneous model. For both models, there is an inverse relationship between the rigidity ratio and the optimal locking depth (linear for the deep CZFM and curved for the shallow CZFM as shown in D. in Fig. 2). As the difference between the CFZMs and the best-fit classic models is smaller than the typical error obtained with non-continuous GPS data (about 1 mm$yr^{-1}$), we cannot distinguish between a shallow locking depth half-space model and a Compliant Fault Zone Model, relying only on geodetic data. Thus it is important to have independent constraints on the locking depth, for instance from the depth extent of microseismicity.

## 3. Space-geodetic constraints on rigidity variations across and within the San Andreas Fault

### 3.1. Global positioning system derived velocities

In 2007 we collected GPS data at sites in Bodega Bay and Tomales Bay (Fig. 1) that were previously observed in 1996–2000 GPS measurements reported by Chen and Freymueller (2002). The data have been processed using the GAMIT/GLOBK processing software (Herring et al., 2006). These velocities are part of the BAVU dataset (d'Alessio et al., 2005) updated with more recent measurements (http://seismo.berkeley.edu/~burgmann/RESEARCH/BAVU/index.html). The stabilization of the network relies on cGPS sites in the Bay Area from the Bay Area Regional Deformation (BARD) network (Houlié and Romanowicz, 2009) and global station data provided by the International GNSS Service (IGS). In Fig. 1, the site velocities are shown with respect to BARD continuous GPS station LUTZ, which is located in the central Bay Area (121.865° W, 37.287° N).

### 3.2. Additional constraints, EDM and PS-SAR data

The use of additional constraints from Electronic Distance Meter (EDM) measurements (Chen and Freymueller, 2002) and PS-SAR data (Funning et al., 2007) helps us to evaluate the inferred models.

EDM measurements rely on a ground based baseline length determination. An electromagnetic signal is emitted from a geodetic site and is reflected back by a remote reflector located at another site. Using a modulated beam, and therefore a band of frequencies wide enough to determine the phase ambiguity (Savage and Prescott, 1973), the analysis of the outcoming and incoming signal phases provides an accurate measurement of the optical path length between the instrument and the reflector. Repeated measurements constrain the deformation rates of a geodetic network. To directly compare these measures to our GPS-derived velocities, we derive velocities from the line-length change rates. We determine the site velocities using the "outer-coordinate" solution method (Prescott, 1981). Assuming that the motion is mostly horizontal and along the fault strike direction, the component of displacement normal to the fault strike is minimized. We prefer this solution to the "inner-coordinate" solution method that minimizes network rotation because a strike-slip fault surface deformation pattern includes rotations. We compute line-length change rates from Chen and Freymueller (2002) and some additional USGS EDM measurements made from the 1970s to the 1980s to determine the velocity field. In Bodega Bay, a total of 17 lines were surveyed between 11 sites. In Tomales Bay, 18 lines were measured between 8 sites. The fault-parallel velocities are shown in Figs. 4 and 5.

To include the EDM line-length-change derived velocities in our data set, we minimize the difference between them and the fault parallel

GPS-derived velocities with respect to station LUTZ. In Tomales Bay, the difference between our GPS-derived velocities and the EDM velocities does not exceed 0.3 $mmyr^{-1}$. In Bodega Bay, the mean difference between our GPS fault-parallel velocities and the EDM-derived motion does not exceed 0.5 $mmyr^{-1}$ at common stations. These differences indicate excellent agreement between the two data sets. The two sites located around 3 km on Fig. 5 (Bodega and Bodega Reference Mark 1) were used to tie the Bodega and Tomales networks. We computed the velocities from the two networks jointly, but the baselines measured to these two sites are mostly parallel to the fault.

### 3.3. The Point Reyes profile

We first develop a simple 2D half-space dislocation model, based on three parallel faults (SAF, RCF and GVF, see Fig. 1). To evaluate the quality of our models, we calculate the $\chi^2$ as the sum of the weighted residuals reduced by the number of data. The best-fit model has a $23\pm1$ $mmyr^{-1}$ slip rate on the SAF, with a $14\pm2$ km locking depth for a $\chi^2=4.33$. We find a $8\pm1$ $mmyr^{-1}$ slip rate on the RCF and $9\pm1$ $mmyr^{-1}$ on the GVF below locking depths of $5\pm3$ km and $4\pm1$ km, respectively, thus the whole system is accommodating $40\pm3$ $mmyr^{-1}$ of fault-parallel displacement (Fig. 3). The measured velocity for the Farallon Island cGPS station (FARB) is about 2 $mmyr^{-1}$ slower than the half-space model velocity. In this case, the modelled far field velocity of the Pacific block interior is $5\pm1$ $mmyr^{-1}$ faster than the observed FARB velocity. However, (d'Alessio et al., 2005) show that the observed velocity of the Farallon Island station with respect to the Pacific plate interior is only $3\pm1$ $mmyr^{-1}$ towards the southeast.

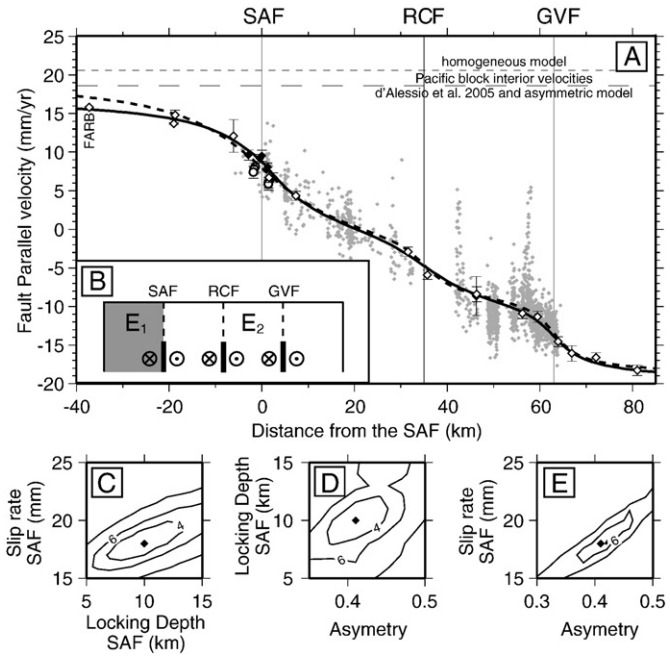


**Fig. 3.** A. Best-fit dislocation models for the Point Reyes profile. The white diamonds are the fault-parallel projected GPS velocities from the BAVU 2 compilation with their associated error bars. The white circles are the fault-parallel projected GPS velocities from this study in Tomales Bay with their associated error bars, the black diamonds correspond to the site velocities in Bodega Bay. The GPS velocities are calculated with respect to station LUTZ (121.865° W, 37.287° N). The grey dots are the PS-SAR data from Funning et al. (2007). The dashed line is the best classic (elastic half-space) dislocation model. The continuous line is our preferred asymmetric model with a K ratio of 0.41. The horizontal long-dashed grey line represents the Pacific block interior velocity predicted by d'Alessio et al. (2005) and by our asymmetric model. The horizontal short-dashed grey line represents the Pacific block interior velocity predicted by our best homogeneous model. B. Geometry of the best-fit dislocation model. The grey-shaded zone corresponds to the high rigidity block. C. Trade-off between the Locking Depth and the Slip Rate on the SAF. Contoured values are the $\chi^2$ values. D. Trade-off between the Asymmetry Ratio and the Locking Depth on the SAF. E. Trade-off between the Asymmetry Ratio and the Slip Rate on the SAF.

We therefore consider asymmetric models with a rigidity contrast across the SAF, fitting the data with Eq. (2). We continue to use the classic half-space dislocation model for the RCF and the GVF. We find that the modelled velocity profile better matches the data and especially the Farallon Islands velocity with a 0.41 K ratio across the SAF. The corresponding $\chi^2$ is 2.63. This model suggests an $18\pm1$ $mmyr^{-1}$ slip rate on the SAF, in agreement with (Freymueller et al., 1999), with a $10\pm2$ km locking depth, a 11 $mmyr^{-1}$ slip rate on the RCF, with a 10 km locking depth and a 9 $mmyr^{-1}$ slip rate on the GVF with a 5 km locking depth. Thus, we infer that the Salinian terrane has a rigidity 1.4 times higher than the Franciscan complex to the east of the SAF. This conclusion is consistent with the type of terrane involved. The rigidity of the Salinian granite should be higher than that of the Franciscan oceanic mixture (Thurber et al., 2007).

There is a significant trade-off between the inferred slip rate on the SAF and the rigidity contrast across the fault, with smaller rigidity contrasts leading to higher inferred slip rates and deeper locking depth (Fig. 3). This trade-off is dominated by the influence of the Farallon Island and Point Reyes station velocities on the fitting process. To obtain a higher slip rate, the rigidity contrasts in the model needs to be decreased and/or the locking depth needs to be increased to produce the Farallon Island velocity, which has a strong weight on the inversion thanks to its low uncertainty.

### 3.4. A compliant fault zone in Bodega Bay

The two dense networks across the SAF located further north, one in Tomales Bay and one in Bodega Bay, allow us to consider if the SAF represents a low-rigidity fault zone. The GPS and EDM-derived velocity gradients across Tomales Bay are similar to those observed at the Point Reyes profile and are well fitted by the asymmetric deformation profile, and we do not find evidence for a compliant fault zone in this area (Fig. 4).

In contrast, at Bodega Bay, we find a strong gradient of GPS velocities in a 2-km-wide zone (black circles in Fig. 5). The EDM data set extends farther west and confirms the change in the deformation gradient (located near −1 and 1 km in Fig. 4). Our preferred model is based on a CFZM, with the previously determined $18\pm1$ $mmyr^{-1}$ slip rate on the SAF, with a $15\pm3$ km locking depth (Fig. 5). The 2-km-wide compliant zone is 50 to 60% weaker than the surrounding medium. But a classic homogeneous model with a 7 km locking depth on the SAF satisfies the near-field data as well, as predicted by the first-order trade-off between locking depth and the compliant fault zone rigidity contrast described in

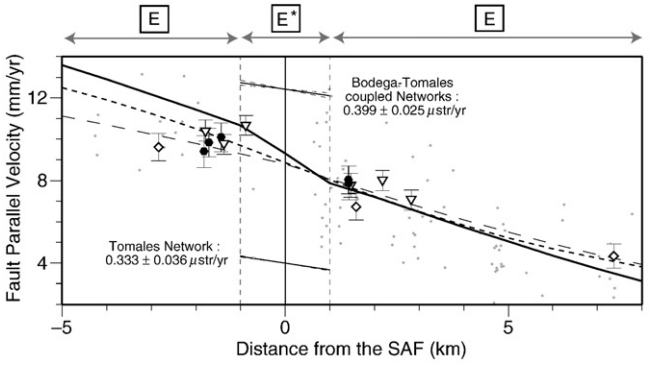


**Fig. 4.** Best dislocation model for the Tomales Bay deformation pattern. The black circles are the fault-parallel GPS velocities in Tomales Bay with their associated error bars with respect to the station LUTZ (121.865° W, 37.287° N), the white diamonds correspond to the Point Reyes profile. The white inverted triangles are fault-parallel EDM-derived velocities from the Tomales Bay. The continuous black line is the Compliant Fault Zone Model that best fits the data in Bodega Bay. The short-dashed line is the best homogeneous model. The long-dashed line is the previous asymmetric model of the Point Reyes profile. The short black lines represent the velocity gradient across Tomales Bay with the associated errors from Chen and Freymueller (2002). The grey arrows show the extent of the compliant fault zone.

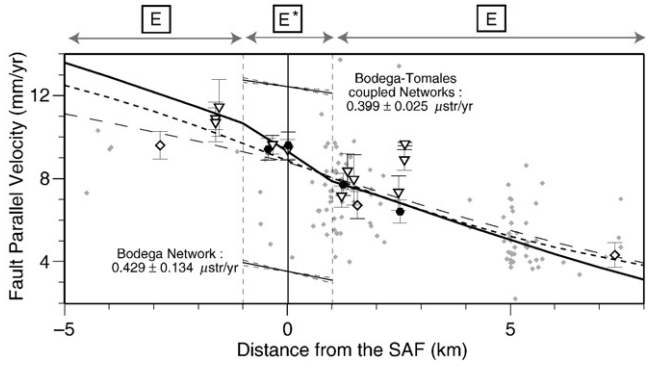


**Fig. 5.** Best dislocation model for the Bodega Bay deformation pattern. The black circles are the fault-parallel GPS velocities in Bodega Bay with their associated error bars with respect to the station LUTZ (121.865° W, 37.287° N), the white diamonds correspond to the Point Reyes profile velocities. The white inverted triangles are fault-parallel EDM-derived velocities from the Bodega Bay network. The grey dots are the PS-SAR data from (Funning et al., 2007) projected onto the profile assuming that the range change is due to fault-parallel motion only. The continuous black line is our preferred Compliant Fault Zone Model, with a ratio $\frac{E^*}{E} = 0.4$. The short-dashed line is the best homogeneous model, with a 7 km locking depth and a 18 mm yr$^{-1}$ slip rate. The long-dashed line is the asymmetric model of the Point Reyes profile. The short black lines represent the velocity gradient through the fault zone in Bodega Bay with the associated errors from Chen and Freymueller (2002). The grey arrows show the extent of the compliant fault zone.

a previous section. Independent evidence of the locking depth can be obtained from the depth distribution of microseismicity, considering that the locking depth is close to the seismic–aseismic transition. Unfortunately, there are very few earthquakes from Point Reyes, up to Bodega Bay, so we cannot directly infer the local seismic–aseismic transition. However, in nearby areas to the south and east the depth above which 90% of the earthquakes occur is around 10–15 km and heat flows measurements in this area suggest a similar locking depth (d'Alessio et al., 2005). Furthermore, studies of the coseismic deformation of the 1906 San Francisco earthquake suggest that the rupture depth exceeded 10 km (Matthews and Segall, 1993; Thatcher et al., 1997; Song et al., 2008). For example, Matthews and Segall (1993) infer a 15-to-20 km transition. Thus, we consider a 10-to-15 km locking depth and introduce a CFZM, assuming that there are no significant changes in the locking depth.

Chen and Freymueller (2002) inferred a low-rigidity fault zone located in the San Francisco Peninsula. The highest rigidity ratio inferred by Chen and Freymueller (2002) ranges between 0.4 and 0.8 in the Black Mountain-Radio Facility network. Combining the data from Tomales and Bodega Bay, they obtained a $0.399 \pm 0.025$ μstr yr$^{-1}$ tensor shear strain rate (Fig. 3). Taking only data from Bodega Bay they find a higher strain rate of $0.429 \pm 0.134$ μstr yr$^{-1}$. We infer a strain rate about twice as high, 0.7 μstr yr$^{-1}$ in a 2-km-wide zone centered on the fault in Bodega Bay corresponding to the location of the compliant zone. The strain accumulation rate seems spatially constant in Tomales Bay, with 0.4 μstr yr$^{-1}$, compared to 0.33 μstr yr$^{-1}$ determined by Chen and Freymueller (2002). This confirms along-fault changes in fault zone properties suggested by Chen and Freymueller (2002).

The PS-InSAR data shown in Fig. 3 are consistent with the Point Reyes profile GPS measurements. The main features inferred from GPS data could have been well resolved using PS-InSAR data only. However, the apparent noise and the limited east–west extent of coverage limit the benefits of using them for a more accurate study. The InSAR data do not aid in resolving the near-fault deformation rates.

## 4. Discussion and conclusions

We consider heterogeneous elastic models, including asymmetry of elastic strength across a fault (Le Pichon et al., 2005), an infinitely deep compliant fault zone (Rybicki and Kasahara, 1977; Chen and Freymueller, 2002) and a shallow compliant fault zone. We show that we cannot distinguish between a deep CFZM and a shallow CFZM only with geodetic data, as differences between the two are less than 1 mm yr$^{-1}$ for a fault slipping at 20 mm yr$^{-1}$.

We then evaluate the trade-off between the inferred locking depth in a half-space model and the rigidity ratio inferred with the CFZM. We show that we can reproduce the effect of any CFZM with a classic half-space model with a shallow locking depth. This suggests that independent information such as seismicity depths or heat flow data is needed to constrain locking depths when considering the effects of compliant fault zones on interseismic deformation. If the locking depth is independently constrained and the slip rate well determined, it becomes possible to discriminate between a shallow CFZM and a deep CFZM by adjusting the rheology ratio to satisfy the near-fault data.

A model inversion allowing for a rigidity contrast across the SAF indicates a 18 mm yr$^{-1}$ slip rate, with a 10 km locking depth and an asymmetry coefficient of 0.41. The Salinian Terrane has a higher rigidity than the Franciscan block. This model is strongly constrained by the velocity of the stations located west of the SAF, especially the two cGPS sites Point Reyes (PTRB) and Farallon Island (FARB). This asymmetry has previously been observed (Prescott and Yu, 1986). We find tradeoffs between the asymmetry ratio, the locking depth and the slip rate on the SAF (Fig. 3) that are in part due to the limited geodetic coverage to the west of the fault. Offshore GPS – acoustic measurements methods (Gagnon et al., 2005) would be needed to better constrain the deformation.

As suggested by Fialko (2006), several alternative models could explain an asymmetric deformation pattern across a strike-slip fault: across-fault contrast in elastic properties of blocks on both sides of the fault (Le Pichon et al., 2005, Jolivet et al., 2008), post-seismic relaxation effects with lateral variations of viscosity (Li and Rice, 1987), additional sub-parallel faults, and non vertical fault geometry (Lisowski et al., 1991). As the last great earthquake in this area was the great 1906 Mw = 7.9 San Francisco earthquake, we can probably eliminate the hypothesis of the viscous post-seismic relaxation effects (Kenner and Segall, 2003). No major structure that can modify the deformation pattern this way has been identified west of the San Andreas Fault in this area. In terms of geometry, the surface trace of the fault indicates a sub vertical fault near the surface. However, (Parsons and Hart, 1999) infer a 60° east dipping San Andreas Fault in the Central Bay Area, coupled to a 70° west dipping Hayward fault. Following (Okada, 1985), we compute the surface displacement field produced by an infinitely deep dipping buried dislocation reproducing the effect of interseismic loading on a dipping SAF and calculate the associated K ratio. To reach the 0.41 observed K ratio, the dipping angle has to be between 70 and 75, which corresponds to a 5–6 km offset of the buried dislocation beneath the SAF to the northeast. However, in the case of a homogeneous elastic medium, (Lisowski et al., 1991) clearly demonstrate that the possible effects of fault geometry cannot be resolved only using surface deformation data. Using relocated seismicity, (Thurber et al., 2007) shows that the SAF is roughly vertical in the northern Bay Area. We therefore consider this asymmetry as the result of a rigidity contrast rather than of a dipping SAF.

North of Point Reyes, in Bodega Bay, a 7 km locking depth homogeneous dislocation model satisfies the data. However, the seismic activity in nearby areas, estimates of 1906 earthquake rupture depths and heat flux measurements suggest that the seismic–aseismic transition is between 10 and 15 km. To match the observed high strain gradient, we introduce a Compliant Fault Zone Model. Our best model suggests a 50 to 60% rigidity decrease in a 2-km-wide compliant zone. In an earlier study, Chen and Freymueller (2002) inferred a low-rigidity near-fault zone located further south, in the San Francisco peninsula. In Bodega Bay, Chen and Freymueller (2002) use the parameter set from the WGCEP99 (1999) which indicates a $24 \pm 1.5$ mm yr$^{-1}$ slip rate and a $11 \pm 1$ km locking depth. Based on a semi-infinite half-space dislocation model, they expect and observe a strain rate of about 0.35–0.4 μstr yr$^{-1}$. This strain rate corresponds to the one obtained

with our best homogeneous model mentioned previously which predicts a 0.4 μstr yr$^{-1}$. However, using both GPS and EDM data we find a strain rate almost twice as high as Chen and Freymueller (2002) over a 2-km-wide near-fault zone, consistent with our compliant fault zone model.

Chen and Freymueller (2002) assume that the rate of strain accumulation is constant in any given time period, which is confirmed by the close agreement between our GPS data set and the EDM-derived velocities. However they also consider a spatially uniform rate of strain accumulation across the whole network. Computing EDM and GPS-derived velocities allows us to resolve deformation-gradient changes across the fault zone. The mean modelled strain rate across a wider (6 km wide) zone centered on the fault is lower, about 0.47 μstr yr$^{-1}$, which is more consistent with Chen and Freymueller (2002).

As we estimate a locking depth ratio between 0.5 and 0.7 and a rigidity ratio between 0.5 and 0.6, we suppose that the compliant fault zone does not extend deeper than the locking depth (Fig. 3 D.). Therefore, this feature may be the result of damage from repeated earthquakes and could be associated with highly fractured and porous fault gauge. Fluids are likely to be driven in the fault zone, decreasing the S-wave velocity. Furthermore, McGuire and Ben-Zion (2005) inferred a damaged fault zone with along-strike, fault-normal and downdip variations in the strength of the velocity contrasts from 20 to 50% in the Bear Valley section of the SAF using relocated seismicity and head waves from a local seismic network. Near-fault seismic studies (Cochran et al., 2009) should be useful to further document the presence and determine the geometry of such a feature, in order to map out changes of fault zone properties along the fault.

## Acknowledgments

This project was funded by the USGS National Earthquake Hazard Reduction Program (NEHRP grants 08HQGR0095 and 07HQAG0031) and NASA (grant NNX08AG50G). We would like to thank J. Freymueller for his help with the GPS site description and data, as well as a very helpful review, and J. Chery for the discussions about ADELI. Berkeley Seismological Laboratory #09-20.

## References

Barbot, S., Fialko, Y., Sandwell, D., 2008. Effect of a compliant fault zone on the inferred earthquake slip distribution. J. Geophys. Res. 113 06.
Ben-Zion, Y., Huang, Y., 2002. Dynamic rupture on an interface between a compliant fault zone layer and a stiffer surrounding solid. J. Geophys. Res. 107 02.
Chen, Q., Freymueller, J.T., March 2002. Geodetic evidence for a near-fault compliant zone along the San Andreas Fault in the San Francisco Bay Area. Bull. Seismol. Soc. Am. 92 (2), 656–671.
Chéry, J., Zoback, M., Hassani, R., 2001. Rheology, strain and stress of the San Andreas Fault in central and Northern California: a 3-d thermomechanical modeling study. J. Geophys. Res. 106 (22), 051–071.
Chinnery, M.A., 1961. The deformation of the ground around surface fault. Bull. Seismol. Soc. Am. 51, 355–372.
Cochran, E.S., Yong-Gang, L., Shearer, P.M., Bardot, S., Fialko, Y., Vidale, J.E., 2009. Seismic and geodetic evidence for an extensive, long-lived fault damage zones. Geology 37 (4), 315–318.
d'Alessio, M.A., Johanson, I.A., Bürgmann, R., Schmidt, D.A., Murray, M.H., 2005. Slicing up the SAn Francisco Bay Area: block kinematics and fault slip rates from gps-derived surface velocities. J. Geophys. Res. 110 (B0640) June.
Fialko, Y., June 2006. Interseismic strain accumulation and the earthquake potential on the southern san andreas fault system. Nature 441 (7096), 968–971.
Fialko, Y., Sandwell, D., Agnew, D., Simons, M., Shearer, P., Minster, B., 2002. Deformation on nearby faults induced by the 1999 Hector Mine Earthquake. Science 297 (5588), 1858–1862.
Freymueller, J.T., Murray, M.H., Segall, P., Castillo, D., 1999. Kinematics of the pacific-north america plate boundary zone, northern california. J. Geophys. Res. 104 (B4), 7419–7442.
Funning, G.J., Bürgmann, R., Ferretti, A., Fumagalli, A., 2007. Creep on the Rodgers creek fault, Northern San Francisco Bay Area from 10 year ps-insar dataset. Geophys. Res. Lett. 34.
Gagnon, K., Chadwell, C.D., Norabuena, E., 2005. Measuring the onset of locking in the Peru–Chile trench with gps and acoustic measurements. Nature 434, 205–208.
Herring, T. A., King, R., McClusky, S. C., September 2006. Documentation of the GAMIT software. Massachusset Institue of Technology, Departement of Earth, Atmospheric, and Planetary Sciences, release 10.3 Edition.
Houlié, N., Romanowicz, B., 2009. Asymmetric deformation across the San Francisco Bay Area faults from GPS observations on the BARD network. Physics of the Earth and Planetary Interiors.
Jolivet, R., Cattin, R., Chamot-Rooke, N., Lasserre, C., Peltzer, G., 2008. Thin-plate modelling of interseismic deformation and asymmetry across the altyn tagh fault zone. Geophys. Res. Lett. 35 (L02309).
Kenner, S.J., Segall, P., 2003. Lower crustal structure in Northern California: implications from strain rate variations following the 1906 San Francisco earthquake. J. Geophys. Res. 108 (B1).
Le Pichon, X., Kreemer, C., Chamot-Rooke, N., 2005. Asymmetry in elastic properties and the evolution of large continental strike-slip faults. J. Geophys. Res. 110 (B03405).
Li, V.C., Rice, J.R., 1987. Crustal deformation in great California earthquake cycles. J. Geophys. Res. 92.
Lisowski, M., Savage, J.C., Prescott, W.H., 1991. The velocity field along the San Andreas Fault in central and southern california. J. Geophys. Res. 96 (B5), 8369–8389.
MacFarland, F.S., Lienkaemper, J.J., J., C.S., Grove, K., 2007. Data from theodolite measurements of creep rates on San Francisco bay region faults, California: 1979–2007. USGS Report Open-File Report 2007–1367.
Matthews, M.V., Segall, P., July 1993. Estimation of depth-dependent fault slip from measured surface deformation with application to the 1906 San Francisco earthquake. J. Geophys. Res. 98 (B7), 12,153–12,163.
McGuire, J., Ben-Zion, Y., Oct 2005. High-resolution imaging of the bear valley section of the san andreas fault at seismogenic depths with fault-zone head waves and relocated seismicity. Geophys. J. Int. 163 (1), 152–164.
Niemi, T.M., Hall, N.T., March 1992. Late holocene slip rate and recurrence of great earthquakes on the San Andreas fault in Northern California. Geology 20, 195–198.
Okada, Y., 1985. Surface deformation due to shear and tensile faults in a half-space. Bull. Seismol. Soc. Am. 75 (4), 1135–1154.
Parsons, T., Hart, P.E., Sep 1999. Dipping San Andreas and Hayward faults revealed beneath San Francisco Bay, California. Geology 27 (9), 839–842.
Peng, Z., Ben Zion, Y., 2006. Temporal changes of shallow seismic velocity around the Karadere-Duzce branch of the north Anatolian fault and strong ground motion. Pure Appl. Geophys. 163, 567–600.
Prescott, W.H., 1981. The determination of displacement fields from geodetic data along a strike slip fault. J. Geophys. Res. 86.
Prescott, W.H., Yu, S.B., 1986. Geodetic measurements of horizontal deformation in the northern San Francisco bay region, California. J. Geophys. Res. 91, 7475–7484.
Rybicki, K., Kasahara, K., 1977. A strike-slip fault in a laterally inhomogeneous medium. Tectonophysics 42, 127–138.
Savage, J.C., Burford, R.O., 1973. Geodetic determination of relative plate motion in central california. J. Geophys. Res. 78.
Savage, J.C., Prescott, W.H., 1973. Precision of geodolite distance measurements for determining fault movements. J. Geophys. Res. 78.
Savage, J.C., Gan, W., Prescott, W.H., Svarc, J.L., 2004. Strain accumulation across the coast ranges at the latitude of San Francisco, 1994–2000. J. Geophys. Res. 109 (B03413).
Schmalzle, G., Dixon, T., Malservisi, R., Govers, R., 2006. Strain accumulation across the Carrizo segment of the San Andreas Fault, California: impact of laterally varying crustal properties. J. Geophys. Res. 111 (B05403).
Song, S.G., Beroza, G.C., Segall, P., April 2008. A unified source model for the 1906 San Francisco earthquake. Bull. Seismol. Soc. Am. 98 (2), 823–831.
Thatcher, W., Marshall, G., Lisowski, M., 1997. Resolution of fault slip along the 470-km-long rupture of the great 1906 San Francisco earthquake and its implications. J. Geophys. Res. 102, 5,353–5,367.
Thurber, C.H., Brocher, T.M., Zhang, H., Langenheim, V.E., 2007. Three-dimensional p wave velocity model for the San Francisco Bay region, California. J. Geophys. Res. 112 (B07313).
WGCEP99, 1999. Working group on California earthquake probabilities, earthquake probabilities in the San Francisco Bay region : 2000–2030. Open-File Rept. 99-517., U.S. Geol. Surv.